

Step-by-step mechanism insights into $\text{TiO}_2/\text{Ce}_2\text{S}_3$ S-scheme photocatalyst for enhanced aniline production with water as proton source

Feiyan Xu

China University of Geosciences <https://orcid.org/0000-0002-5763-128X>

Kai Meng

Wuhan University of Technology <https://orcid.org/0000-0001-6127-2753>

Shuang Cao

Wuhan University of Technology

Chen-Hui Jiang

University of Science and Technology of China

Tao Chen

University of Science and Technology of China <https://orcid.org/0000-0002-3483-8341>

Jingsan Xu (✉ jingsan.xu@qut.edu.au)

Queensland University of Technology <https://orcid.org/0000-0003-1172-3864>

Jiaguo Yu

China University of Geosciences

Article

Keywords: heterostructured photocatalysts, photocatalytic hydrogenation, S-scheme, nitrobenzene hydrogenation

Posted Date: September 10th, 2021

DOI: <https://doi.org/10.21203/rs.3.rs-876600/v1>

License:   This work is licensed under a Creative Commons Attribution 4.0 International License.

[Read Full License](#)

Version of Record: A version of this preprint was published at ACS Catalysis on December 14th, 2021. See the published version at <https://doi.org/10.1021/acscatal.1c04903>.

Abstract

Exploring new heterostructured photocatalysts for photocatalytic hydrogenation reaction with water as proton source and investigating the corresponding intrinsic step-by-step mechanism are of great interests. Here we develop a novel S-scheme heterojunction through theoretical design and implemented by solvothermal growth of Ce_2S_3 nanoparticles onto electrospun TiO_2 nanofibers. The low-dimensional (0D/1D) heterostructure unveils enhanced photocatalytic activity for aniline production by nitrobenzene hydrogenation with water as proton source. Density functional theory (DFT) calculations indicate the electrons transfer from Ce_2S_3 to TiO_2 upon hybridization due to their Fermi level difference and creates an internal electric field at the interface, driving the efficient separation of the photoexcited charge carriers, which is authenticated by *in-situ* X-ray photoelectron spectroscopy along with femtosecond transient absorption spectroscopy. The step-by-step reaction mechanism of the photocatalytic nitrobenzene hydrogenation to yield aniline is revealed by *in-situ* diffuse reflectance infrared Fourier transform spectroscopy, associated with DFT computational prediction.

Introduction

Photocatalytic hydrogenation with water as proton source has been explored as a promising approach in organic synthesis and is widely applied in current pharmaceutical and fine chemical industries.^{1,2} Aniline is one type of important organic compounds and intermediates in the production of pharmaceuticals, food additives, agrochemicals, dyes and so on.^{3,4} In the past years, catalytic hydrogenation has been widely studied for reducing nitrobenzene to aniline using Pt, Pd, Au or transition metals as cocatalysts, which usually requires harsh reaction conditions and greatly increases the product cost and fabrication difficulty.⁵⁻⁹ In addition, the intrinsic hydrogenation mechanism, which is important to uncover the underlying reasons for the improved photocatalytic activity, was neglected up to now. Thus, developing new photocatalysts to achieve efficient photocatalytic hydrogenation activity with water as proton source and understanding the reaction mechanism are recognized as major challenges.

TiO_2 nanofibers are used as a matrix with intriguing properties featuring short charge transport length, inert aggregation and increased surface area.¹⁰⁻¹³ Nevertheless, like other mono-component photocatalysts, the photocatalytic efficiency of unitary TiO_2 nanofibers is still far away from practical application due to the rapid recombination rate of photogenerated electron/hole pairs.¹⁴⁻¹⁸ A traditional type-II heterojunction is widely used for the electron/hole separation of a photocatalyst. However, its asserted charge-transfer mode fails to separate photogenerated charge carriers in terms of dynamics. Moreover, photoinduced electrons and holes accumulate on oxidation and reduction photocatalysts, respectively, causing weakened redox ability from a thermodynamic perspective.¹⁹⁻²² Recently, a step-scheme (S-scheme) heterojunction that is composed of oxidation photocatalyst and reduction photocatalyst was developed, which offers a feasible solution to the dilemma that traditional type-II heterojunction confronts.^{23,24} In the S-scheme heterojunction, the futile photogenerated electrons and holes are eliminated through recombination, while the powerful electrons with strong reduction ability in

the conduction band (CB) of reduction photocatalyst and the holes with strong oxidation ability in the valance band (VB) of oxidation photocatalyst are preserved to engage in photocatalytic reactions. Such transfer pathway of the photogenerated charge carriers is distinct from that of traditional type-II heterojunctions, which facilitates efficient charge carrier separation and, in the meantime, remains their strong redox capability.²⁵⁻²⁸ In macroscopic level, the charge-transfer route (electrons transfer from low CB to high CB) in the heterojunction resembles a “step”, thus is named step-scheme (S-scheme) heterojunctions.¹⁹

TiO₂ is recognized as an oxidation photocatalyst with relatively weak reduction ability. To improve its photocatalytic hydrogenation performance, it is required to explore a reduction photocatalyst with relatively negative CB position to combine with TiO₂ and form a preferable heterojunction. Ce₂S₃, a promising reduction photocatalyst with a bandgap of 2.1 eV, has been barely investigated for catalyzing organic transformations. The CB and VB positions of Ce₂S₃ are located at - 0.91 eV and 1.19 eV (*vs.* NHE), respectively.²⁹⁻³¹ Our calculation on work function of TiO₂ and Ce₂S₃ (Supplementary Fig. 1) indicates upon the combination of the two materials, an S-scheme heterojunction could be formed. Experimentally, the TiO₂/Ce₂S₃ heterostructure was synthesized by electrospinning, low temperature solvothermal and calcination methods (see Methods section for details). Such novel hybrid nanofibers show boosted aniline production by photocatalytic hydrogenation of nitrobenzene with water as hydrogen source. *In-situ* X-ray photoelectron spectroscopy (XPS) and femtosecond transient absorption spectroscopy (fs-TAS), as well as kinetic profiles were investigated to verify the S-scheme charge transfer pathway. *In-situ* diffuse reflectance infrared Fourier transform spectroscopy (DRIFTS) together with density functional theory (DFT) calculations have shed light on the step-by-step reaction mechanism toward hydrogenation of nitrobenzene to aniline. Isotope labeling experiment confirmed water being the sole hydrogen donor. This work provides a unique mechanism viewpoint for efficient aniline production by nitrobenzene hydrogenation with water as proton source driven by S-scheme charge-transfer route within TiO₂ nanofiber-based photocatalyst.

Results And Discussion

Characterization of TiO₂/Ce₂S₃ heterostructure. The obtained TiO₂/Ce₂S₃ heterojunctions were denoted as TC_x, where T and C represent TiO₂ nanofiber and Ce₂S₃ nanoparticle, respectively; *x* is the mole percentage of Ce₂S₃ with respect to TiO₂. As can be seen from the field emission scanning electron microscopy (FESEM) and transmission electron microscopy (TEM) images, Ce₂S₃ nanoparticles uniformly deposited on the surface of TiO₂ nanofibers (Fig. 1a, b). The phase structure of the hybrid nanofibers was determined by X-ray diffraction (XRD) (Supplementary Fig. 2) and high-resolution transmission electron microscopy (HRTEM). Two sets of lattice spacings of 0.352 and 0.325 nm, corresponding to anatase (101) and rutile (110) planes, respectively, were observed in HRTEM image (Supplementary Fig. 3b). The lattice spacings of TiO₂, as well as Ce₂S₃, appeared in the HRTEM image simultaneously (Fig. 1c) for the hybrid nanofibers. The energy-dispersive X-ray spectroscopy (EDX)

spectrum (Fig. 1d) and the high-angle annular dark field (HAADF) image (Fig. 1e) both revealed the existence of Ti, O, Ce and S elements in the composite sample TC5, further confirming the formation of TiO₂/Ce₂S₃ nano hybrids.

The surface chemical states of the samples were studied by X-ray photoelectron spectroscopy (XPS). Two symmetrical peaks (Ti 2*p*_{3/2} and Ti 2*p*_{1/2}) assigning to Ti⁴⁺ ions can be seen in the high resolution XPS spectra of Ti 2*p* of TiO₂ and TC5 (Fig. 2a). The Ce 3*d* spectra can be resolved into two pairs of spin-orbit peaks as shown in Fig. 2b. The peaks located at 885.8 and 903.9 eV were attributed to the state of Ce³⁺ in Ce₂S₃. The other pair of peaks at 882.4 and 900.5 eV were assigned to the satellite peak of Ce. Noticeably, in TC5 sample, the binding energies (BEs) of Ti 2*p* and O 1*s* (Supplementary Fig. 4a) shifted 0.2 eV towards a lower value comparing with those of pristine TiO₂; conversely, the BEs of Ce 3*d* and S 2*p* (Supplementary Fig. 4b) of TC5 became more positive in comparison with those of Ce₂S₃, implying the electrons transfer from Ce₂S₃ to TiO₂ upon hybridization in dark. Such electron transfer between TiO₂ and Ce₂S₃ resulted in an internal electric field (IEF) pointing from Ce₂S₃ to TiO₂, which will drive the efficient separation of photoinduced charge carriers as revealed by *in-situ* XPS (discussed below) and form S-scheme TiO₂/Ce₂S₃ heterojunctions to promote the photocatalytic performance.

The difference of work functions (Φ), which can be explored by the contact potential difference (CPD) between the samples and the standard gold tip of Kelvin probe instrument, is an essential parameter leading to the electron transfer within duplicate semiconductor heterostructures in dark. As shown in Fig. 2c, the CPD of TiO₂, TC5 and Ce₂S₃ reached a stable value in dark. The work function (Φ) and Fermi level (E_F) can be calculated by the following equations:

$$\Phi = \Phi_{\text{tip}} + e \times \text{CPD} \quad (1)$$

$$E_F = -\Phi \quad (2)$$

where e represents the electron charge, Φ_{tip} is the standard work function of the gold tip (~ 4.25 eV).³² As shown in Fig. 2d, the work functions of TiO₂, TC5 and Ce₂S₃ were estimated to be 4.31, 4.27 and 3.99 eV, respectively, indicating that the Fermi level of TiO₂ is lower than that of Ce₂S₃ (-4.31 vs. -3.99 eV), consistent with our above DFT analysis (Supplementary Fig. 1). Once they begin to contact with each other, the electrons tend to transport from Ce₂S₃ to TiO₂, forcing the phases to reach a same Fermi level (-4.27 eV) and thus creates an IEF at TiO₂/Ce₂S₃ interfaces directing from Ce₂S₃ to TiO₂ (Fig. 2d), which is in accordance with above XPS results.

Insights into charge separation mechanism of S-scheme heterojunction. To explore the charge separation mechanism, the band structures of TiO₂ and Ce₂S₃ were first to investigate. The VB XPS spectra showed that the energy levels of valence band maximum (VBM) of TiO₂ and Ce₂S₃ were 2.67 and 0.95 eV (vs. NHE), respectively (Supplementary Fig. 5a). The flat-band potentials of TiO₂ and Ce₂S₃ were 0.07 and 0.05 eV (vs. NHE), respectively, derived from the Mott-Schottky plots (Supplementary Fig. 5b). Combined

with the band gap of TiO₂ (3.27 eV) and Ce₂S₃ (2.01 eV) (Supplementary Fig. 5c), the positions of VBM and the conduction band minimum (CBM) of TiO₂ and Ce₂S₃ were derived as shown in Supplementary Fig. 5d.

Based on the above XPS, DFT calculation and CPD analyses, the Fermi level of TiO₂ was lower than that of Ce₂S₃, inducing the electrons to flow from Ce₂S₃ to TiO₂ upon contact with each other, forming an IEF directing from Ce₂S₃ to TiO₂, meanwhile bending the energy bands of TiO₂ and Ce₂S₃ at interfaces. Upon light excitation, the VB electrons of TiO₂ and Ce₂S₃ both jumped to their CBs. Driven by the interfacial IEF and bent bands, the photoinduced electrons in TiO₂ CB transferred to Ce₂S₃ VB spontaneously and recombined with the holes in Ce₂S₃ VB. While the powerful photogenerated electrons in Ce₂S₃ CB and the holes in TiO₂ VB were preserved to engage in photocatalytic reactions. Such charge-transfer route resembles “step” in macroscopic level (from TiO₂ CB to Ce₂S₃ CB) and letter of “N” in microscopic level, following the S-scheme charge transfer pathway (Fig. 3a), which can efficiently separate the photogenerated electron-hole pairs and in the meantime maintain the high redox ability of electrons in Ce₂S₃ CB and holes in TiO₂ VB, respectively. Therefore, the obtained S-scheme TiO₂/Ce₂S₃ heterojunctions will endow excellent photocatalytic nitrobenzene hydrogenation activity.

To evidence the charge-transfer route in S-scheme heterojunction more intuitively, *in-situ* XPS spectra were measured under light irradiation (Fig. 2a, b and Supplementary Fig. 4). Obviously, the BEs of Ti 2*p* and O 1*s* for TC5 shifted positively, while the BEs of Ce 3*d* and S 2*p* of TC5 showed a negative shift under light irradiation, with reference to the corresponding BEs in the XPS spectra in dark. Such shifts soundly proved that the photoexcited electrons in TiO₂ CB transferred to Ce₂S₃ VB under light irradiation. From macroscopic perspective, electrons in the TiO₂/Ce₂S₃ nanohybrids steps from low energy level (TiO₂ CB) to high energy level (Ce₂S₃ CB), following the S-scheme charge-transfer pathway.^{33–35}

The S-scheme charge transfer dynamics was further investigated by the femtosecond transient absorption spectroscopy (fs-TAS), which is widely recognized as the most powerful method to disclose the photoinduced charge transport mechanism in semiconductors.^{36–38} As depicted in Fig. 3b-e, a pronounced negative peak at 645 nm was observed for both TiO₂ and TiO₂/Ce₂S₃ nanohybrids (TC5), which can be interpreted as the stimulated radiation of TiO₂ and corresponded to the recombination of photoinduced electrons and holes.^{39–41} This assignment was further confirmed by the experiment performed in the presence of an electron scavenger (AgNO₃), in which the signal virtually disappeared (Supplementary Fig. 6), indicating that the photogenerated electrons were trapped by the electron scavenger with no electrons to recombine with the holes. Through monitoring the signal strength at 645 nm with different delay times, we noticed that the composite sample TC5 exhibited weaker intensity than pure TiO₂ nanofibers, suggesting less recombination of photocarriers in TC5 than in pristine TiO₂. Moreover, the spectroscopic nature of the charge carriers of TC5 altered at a much slower rate after 50 ps, indicating a relatively slow recombination of electrons and holes over the nanohybrids. The decay kinetics at 645 nm within 100 ps of TiO₂ and TC5 were fitted and analyzed using a tri-exponential

function and the results were presented in Fig. 3f and Table 1. In general, the whole series of process can be partitioned into three-time regions. The shortest lifetime (τ_1) corresponds to the process of electron trapping, which means the photoexcited electrons in CB quickly relax into the impurity state of Ti^{3+} first, and this process is the fastest. The nanohybrids TC5 possessed more Ti^{3+} than pure TiO_2 as evidenced by electron spin resonance (ESR) spectra shown in Supplementary Fig. 7. Herein, for TC5, more photogenerated electrons in TiO_2 CB were trapped by the impurity state, leading to longer lifetime of τ_1 (3.92 ns) in comparison with pure TiO_2 (1.88 ns). The lifetime τ_2 is assigned to the process of interfacial electron transfer from the impurity state of TiO_2 to Ce_2S_3 VB, and τ_3 can be ascribed to the recombination of holes in TiO_2 VB with electrons at the impurity state. When Ce_2S_3 nanoparticles deposited on TiO_2 nanofibers, the photoexcited electrons in TiO_2 can find a new relaxation channel *via* Ce_2S_3 , which leads to longer lifetime of τ_2 (TC5: 43 ns, TiO_2 : 27 ns) (inset of Fig. 3f) and thus shorter lifetime of τ_3 (TC5: 39 ns, TiO_2 : 103 ns) (Fig. 3f) comparing with pristine TiO_2 . It is worth noting that as the delay time prolonged, the kinetic trace curves rose tardily again, especially for TC5 (Supplementary Fig. 8), which was owing to the fact that free electrons trapped at the impurity state slowly released later and thus prolonged the lifetime. Therefore, it is apparent that the rapid surface trapping of the electrons as well as a timely and spatial charge separation occurred in the TiO_2/Ce_2S_3 nanohybrids led to the suppressed electron-hole recombination and supported the formation of S-scheme charge transfer between TiO_2 and Ce_2S_3 . Accordingly, the schematic illustration of the S-scheme charge transfer mechanism in TiO_2/Ce_2S_3 nanohybrids was depicted in Fig. 3g.⁴²

Table 1
Parameters derived from fitted kinetics at 645 nm within 100 ps for TiO_2 and TC5.

Sample	τ_1 (ps)	τ_2 (ps)	τ_3 (ps)
TiO_2	1.88	27	103
TC5	3.92	43	69

The transient photocurrent responses for TiO_2 and TC5 were recorded to reaffirm the charge separation between TiO_2 and Ce_2S_3 (Supplementary Fig. 9a), where the composite TC5 exhibited a higher photocurrent density compared with pure TiO_2 , testifying the superior charge separation efficiency of TiO_2/Ce_2S_3 nanohybrids. Interestingly, under initial light irradiation, TC5 exhibited an obvious photocurrent decrease; when light was switched off, the photocurrent dropped steeply then increased smoothly. Such unique phenomenon was supposed to be induced by the trapping of electrons by the impurity state of Ti^{3+} . Upon light irradiation, the electrons first jumped from VB to CB, then quickly

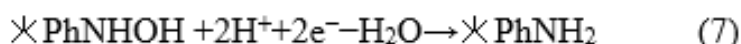
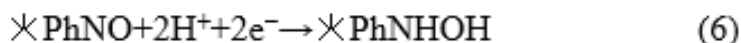
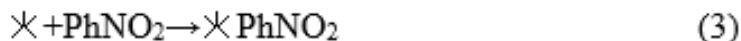
trapped by the impurity state, resulting in the instantaneous decrease of photocurrent. Accordingly, when the light was off, the photocurrent declined then rose steadily, indicating that the trapped electrons gradually migrated to the cathode. Herein, the electron trapping at the impurity state is beneficial to the separation of photogenerated electron-hole pairs and can improve the photocatalytic performance, as also evidenced by above fs-TAS results. Additionally, the electrochemical impedance spectra (EIS) of TiO_2 , TC5 and Ce_2S_3 (Supplementary Fig. 9b) showed that the composite TC5 exhibited the smallest semicircle in comparison with pristine TiO_2 and Ce_2S_3 , indicating that the $\text{TiO}_2/\text{Ce}_2\text{S}_3$ nanohybrids revealed lowest charge transfer resistance. The polarization curves of TiO_2 , TC5 and Ce_2S_3 under UV light irradiation (Supplementary Fig. 9c) showed that the overpotential for TC5 was lower than that of TiO_2 and Ce_2S_3 , indicating better reduction capability of $\text{TiO}_2/\text{Ce}_2\text{S}_3$ nanohybrids. These electrochemical results proved that Ce_2S_3 nanoparticles could form S-scheme heterojunction with TiO_2 nanofibers promoting the electron transfer and separation of electron-hole pairs. Based on these analyses, it is expected that the $\text{TiO}_2/\text{Ce}_2\text{S}_3$ S-scheme heterojunction shall exhibit excellent performance toward photocatalytic hydrogenation of nitrobenzene to aniline.

Photocatalytic nitrobenzene hydrogenation over $\text{TiO}_2/\text{Ce}_2\text{S}_3$ hybrids. The photocatalytic nitrobenzene hydrogenation performance of the resultant samples was evaluated by using H_2O as hydrogen source. Controlled experiments demonstrated that no aniline was detected in dark or in the absence of either H_2O or nitrobenzene, indicating that the light irradiation, input H_2O and nitrobenzene were indispensable for the photocatalytic hydrogenation reaction. As shown in Fig. 4a and b, pristine TiO_2 nanofibers and Ce_2S_3 nanoparticles showed relatively lower production rate of aniline owing to the rapid recombination and lower utilization of photoinduced charge carriers. After depositing Ce_2S_3 nanoparticles on TiO_2 nanofibers, the concentration of aniline was greatly enhanced and achieved the maximum yield of 99% when TC5 was irradiated for 90 min. Such excellent photocatalytic hydrogenation performance of $\text{TiO}_2/\text{Ce}_2\text{S}_3$ nanohybrids was in our expectation and outperformed most photocatalysts with deposited noble metals as cocatalysts.⁴³⁻⁴⁵ Nevertheless, further loading of Ce_2S_3 (e.g., TC7) would deteriorate the photocatalytic activity of the nanohybrids because the overloading could shield the light absorption of TiO_2 . Note that the preserved holes in TiO_2 VB oxidized triethanolamine (TEOA) to produce diethanolamine (DEA), prolonging the lifetime of electrons in Ce_2S_3 CB. To determine the hydrogen source of the hydrogenation reaction, an isotope-labeling experiment was conducted by replacing H_2O with D_2O over TC5. As shown in Fig. 4c, the total ion chromatographic peak at 3.79 min corresponded to aniline, which produced two main ion signals, as well as some fragment peaks in the mass spectrum. The m/z values of 95 and 67 were assigned to aniline ($\text{C}_6\text{H}_5\text{D}_2\text{N}$) and the fragmentation benzene of aniline ($\text{C}_6\text{H}_5\text{D}$), respectively, verifying that the hydrogen source was the input water rather than any other hydrogen-containing agents such as triethanolamine or organic solvents. To better demonstrate the liability of the resultant samples, we evaluated the recyclability and stability of the catalyst TC5 for photocatalytic hydrogenation. As shown in Supplementary Fig. 10, after five-time cycles, neglecting the influence of the catalyst loss during washing and drying processes, the decay of the aniline yield was

hardly perceptible. The applied photocatalyst showed no detectable change in phase and morphology, evidenced by the XRD pattern (Supplementary Fig. 11), FESEM and TEM images (Supplementary Fig. 12). The chemical states were consistent with those of the fresh one as revealed by XPS spectra in Supplementary Fig. 13. All the results suggest the acceptable photostability of TiO₂/Ce₂S₃ nanohybrids during the photocatalytic nitrobenzene hydrogenation reaction.

The adsorption of the reactant and the desorption of the product on the heterostructured photocatalyst were calculated using DFT theory. Supplementary Fig. 14 compared the optimized H₂O and nitrobenzene molecules adsorbed on TiO₂ and Ce₂S₃. The adsorption energy (E_{ad}) of H₂O on anatase TiO₂ (- 0.9 eV), rutile TiO₂ (- 1.16 eV) and Ce₂S₃ (- 1.01 eV) was comparable, indicating that H₂O was adsorbed equally on TiO₂ and Ce₂S₃ from a thermodynamic perspective. However, Ce₂S₃ was located at the outer shell of TiO₂ nanofibers. H₂O had shorter diffusion distance to reach Ce₂S₃, enabling preferential adsorption on the Ce₂S₃ rather than the inner TiO₂ in a kinetic view. Further investigation shows that nitrobenzene preferred adsorption on Ce₂S₃ with more negative adsorption energy (- 1.76 eV) than on anatase TiO₂ (- 1.34 eV) or rutile TiO₂ (- 1.46 eV), suggesting that Ce₂S₃ was the prior adsorption site for both reactants. We also investigated the desorption energy of aniline on each photocatalyst (Supplementary Fig. 15). The aniline demanded less energy to desorb from Ce₂S₃ (0.46 eV) than from rutile (1.13 eV) or anatase TiO₂ (0.49 eV). The results manifest that Ce₂S₃ nanoparticles are in favor of both reactant adsorption and product desorption, which definitely behave as the active sites (not TiO₂ nanofibers) for the photocatalytic hydrogenation of nitrobenzene.

The intermediate species was explored with *in-situ* DRIFTS to uncover the mechanism of the photocatalytic hydrogenation reaction (Fig. 4d). As H₂O and nitrobenzene vapors were introduced into the system in dark, there appeared characteristic absorption bands belonging to the adsorbed H₂O (2350 cm⁻¹) and nitrobenzene (2860 and 2965 cm⁻¹). Their intensities gradually increased with the adsorption time, confirming the simultaneous adsorption of H₂O and nitrobenzene on the photocatalyst. Upon light irradiation, new absorption band appeared at 3230 cm⁻¹ corresponding to (N) - OH species, while the bands at 1653 and 3435 cm⁻¹ could be assigned to N = O and -NH, which belonged to the intermediate species during the photocatalytic hydrogenation reaction. In addition, the -NH₂ absorption band of aniline was also detected at 1157 cm⁻¹ under light irradiation, suggesting the production of aniline. The most likely pathway for photocatalytic hydrogenation of nitrobenzene to aniline was proposed as follows (Supplementary Fig. 16):



where the asterisk denotes the photocatalyst and Ph represents the benzene ring.

To confirm the reaction mechanism, we performed DFT calculations on Gibbs free energy change of each elementary reaction (Supplementary Fig. 16). As shown in Fig. 4e and Supplementary Fig. 17, the photocatalytic nitrobenzene hydrogenation reaction was an exothermic and spontaneous process, indicating that the proposed hydrogenation pathway is reasonable in a thermodynamic view. However, the desorption of aniline was endothermic and required an extra energy, which was the rate-limiting step for all the samples. As mentioned above, the desorption energy of aniline on Ce_2S_3 surface (0.46 eV) was lower than that on anatase and rutile TiO_2 surfaces (0.49 and 1.13 eV) (Fig. 4f), which implied that Ce_2S_3 is more beneficial for aniline desorption and promotes the photocatalytic hydrogenation reaction.

In summary, we have constructed a unique $\text{TiO}_2/\text{Ce}_2\text{S}_3$ S-scheme heterojunction photocatalyst for enhanced aniline production by nitrobenzene hydrogenation with water as proton source. DFT calculation and CPD results revealed the Fermi level of TiO_2 was lower than that of Ce_2S_3 , implying electrons transfer from Ce_2S_3 to TiO_2 as evidenced by XPS, which bent the bands and created an IEF at the interfaces. Under light irradiation, the photoinduced electrons in TiO_2 CB would immigrate to Ce_2S_3 VB driven by the bent bands and IEF, confirming the formation of S-scheme heterojunction between TiO_2 and Ce_2S_3 and achieving efficient separation of photocarriers, thus improve the photocatalytic performance greatly. *In-situ* XPS and fs-TAS spectra further confirmed the charge-transfer route of S-scheme heterojunction. *In-situ* DRIFTS together with DFT calculations shed light on the step-by-step photocatalytic reaction mechanism toward hydrogenation of nitrobenzene to aniline intuitively and detailedly. Isotope (D_2O) tracer results verified that the hydrogen was from water rather than from other hydrogen-containing agents. This work provides a pathway for the design of S-scheme photocatalysts and mechanism insights into boosted photocatalytic nitrobenzene hydrogenation performance.

Methods

Synthesis of electrospun TiO₂ nanofibers. All the chemicals were of analytic grade. Poly(vinyl pyrrolidone) (PVP, MW = 1300000) was purchased from Tianjin Bodi Chemical Co., Ltd and others were purchased from Shanghai Chemical Company. Typically, tetrabutyl titanate (TBT, 4.0 g) and PVP (1.5 g) were added into ethanol (20.0 g) and acetic acid (4.0 g) to form a transparent pale-yellow solution after magnetic stirring for several hours under room temperature. Then the solution was transferred into a 20 mL syringe in an electrospinning setup. The voltage, solution feeding rate and needle-to-collector distance of electrospinning were set to be 20 kV, 2.5 mL h⁻¹ and 10 cm, respectively. Afterwards, the collected TiO₂ precursor was annealed at 550°C for 2 h with a heating rate of 2°C min⁻¹ in air.

Preparation of TiO₂/Ce₂S₃ heterostructures. Typically, 0.03 mmol of Ce(NO₃)₃·6H₂O (equivalent to 1 mol% Ce₂S₃) and 0.06 mmol of hexamethylenetetramine were dissolved in 30 mL of water and 30 mL of ethanol to form a transparent solution. Then 1.5 mmol of TiO₂ nanofibers were added into the above solution to form a suspension. The suspension was transferred to a 100 mL Teflon-lined stainless steel autoclave and then heated in an oven at 75°C for 12 h. The solid product was washed with deionized water and ethanol for three times and then dried at 60°C in air. The obtained product was the TiO₂/CeO₂ precursor. For comparison, the precursor containing 0.5, 3, 5 and 7 mol% CeO₂ were also synthesized by varying the amounts of Ce(NO₃)₃·6H₂O and hexamethylenetetramine. To synthesize TiO₂/Ce₂S₃ heterostructures, the TiO₂/CeO₂ precursors (~ 20 mg) were mixed with 0.1 g of thiocarbamide and calcined at 600°C for 2 h at a heating rate of 10°C min⁻¹ in Ar atmosphere. The obtained TiO₂/Ce₂S₃ heterostructures were labelled as TC_x, where T and C represent TiO₂ and Ce₂S₃, respectively; *x* is the mole percentage of Ce₂S₃ in TiO₂/Ce₂S₃ hybrids (*x* = 0.5, 1, 3, 5 and 7).

Characterization. XRD patterns were performed on a D/Max-RB X-ray diffractometer (Rigaku, Japan) with Cu K_α radiation. The morphology of samples was observed by a field emission scanning electron microscope (JSM 7500F, Japan). TEM images were recorded on a Titan G2 60–300 electron microscope equipped with an EDX spectrometer. UV-visible DRS was collected on a Shimadzu UV-2600 UV-visible spectrophotometer (Japan). XPS was carried out on a Thermo ESCALAB 250Xi instrument with Al K_α X-ray radiation. *In-situ* XPS was conducted under the same condition except that UV light irradiation was introduced. The steady-state PL emission spectra were collected on a Fluorescence Spectrophotometer (F-7000, Hitachi, Japan). TRPL spectra were recorded on a fluorescence lifetime spectrophotometer (FLS 1000, Edinburgh, UK) at an excitation wavelength of 375 nm. The *in-situ* FTIR analyses were carried out on Nicolet iS 50 spectrometer (Thermo fisher, USA) in two sequential steps. Initially, the photocatalyst was allowed to adsorb nitrobenzene and H₂O for 1 h in dark. The mixture of nitrobenzene and H₂O vapors were purged into the sample chamber with the continuous N₂ flow, which continuously passed through the solution containing nitrobenzene, H₂O and TEOA. Then, a 3 W-LED light of 365 nm was turned on and illuminated for 2 h to *in-situ* monitor the photocatalytic hydrogenation of nitrobenzene. For CPD measurement, the samples were prepared by coating them on an ITO substrate and connected to the standard gold tip by the inner circuit. Electron paramagnetic resonance (EPR) was performed on an ESR spectrometer (MEX-nano, Bruker) with a modulation frequency of 100 kHz and a microwave power of 15

mW. Electrochemical measurements were conducted on an electrochemical analyzer (CHI660C, CH Instruments, Shanghai), in which Pt wire, Ag/AgCl (saturated KCl) and 0.5 M Na₂SO₄ solution functioned as counter electrode, reference electrode and electrolyte, respectively. Polarization curves were obtained by linear sweep voltammetry (LSV) with a scan rate of 5 mV s⁻¹. All applied potentials were converted with respect to reversible hydrogen electrode (RHE), namely, $E_{\text{RHE}} = E_{\text{Ag/AgCl}} + 0.059 \text{ pH} + 0.197 \text{ V}$. Overpotential (η) = 0 - E_{RHE} .

Femtosecond Transient Absorption Spectroscopy (fs-TAS) was performed on a pump-probe system (Helios, Ultrafast System) with the maximum time delay of ~ 8 ns using a motorized optical delay line under ambient conditions. The pump pulses at 350 nm (~ 20 μW average power at the sample) were delivered by an ultrafast optical parametric amplifier (OPera Solo) excited by a regenerative amplifier (Coherent Astrella, 800 nm, 35 fs, 5 mJ, 1 kHz), seeded with a mode-locked Ti:sapphire oscillator (Coherent Vitara, 800 nm, 80 MHz) and pumped with a LBO laser (Coherent Evolution-50C, 1 kHz system). A small amount of 800 nm femtosecond pulses from the regenerative amplifier were used to pump a sapphire crystal to create a 420–800 nm white light continuum as probe pulses. The TA spectra were fitted with *Surface Explorer* software by the convoluted multi-exponential function:

$$\Delta A(t) = e^{-\left(\frac{t-t_0}{t_p}\right)^2} * \sum_{i=1}^N A_i e^{-\frac{t-t_0}{\tau_i}}$$

9

where t is the probe time delay, t_0 is time zero, $t_p = IRF/(2 \cdot \ln 2)$, IRF is the width of instrument response function (full width half maximum), A_i and τ_i are amplitudes and decay times, respectively, * is convolution. The minimum number of components N to satisfactorily fit the experimental data is three.

Photocatalytic activity testing. The photocatalytic activity testing was performed in a 50 mL Quartz reactor. Typically, 15 mg of catalyst, 120 μL /100 mL of nitrobenzene, 4 mL of 1,4-dioxane, 1 mL of ultrapure water and 0.5 mL of TEOA were added in the reactor. Then the reactor was sealed and purged with N₂ for 15 times by Multi-Atmosphere Controller (PLA MAC 1005, Beijing PerfectLight, China). Afterwards, the reactor was irradiated with a LED light (wavelength: 365 nm, PCX-50C Discover, Beijing PerfectLight, China) at 30°C. After reaction, the mixture was filtered to remove solid catalysts and then analyzed by a gas chromatograph (GC-2014C, Shimadzu Corp., Japan) equipped with a flame ionization detector (FID) and a capillary column (HP-5, 30 m \times 0.32 mm \times 0.25 μm , Agilent Technologies, USA). The column was maintained at 70°C for 8 min, then heated to 250°C at 40°C min⁻¹ and maintained for another 2 min. The pressure of carrier gas was set to 80 kPa. The temperatures of the injector and the detector were set to be 250 and 270°C, respectively. For reusability testing, the used catalysts were washed twice by ethanol, dried at 60°C in a vacuum oven and reused in the next reaction cycle. The isotope labeling experiment was conducted by using D₂O (99.9%, Macklin) instead of ultrapure water as the hydrogen source. The protocol of photocatalytic activity testing was the same with that mentioned above. The products were analyzed by gas chromatography-mass spectrometry (TRACE 1300 and ISQ

7000, Thermo scientific, USA) equipped with the capillary column (HP-5, 30 m× 0.32 mm× 0.25 μm, Agilent Technologies, USA). Helium was the carrier gas with pressure set to 60 kPa. The temperatures of the injector, ion source and MS transfer line were set to be 250, 230 and 250°C, respectively.

Computational details. The DFT calculations were carried out by using the Vienna Ab initio Simulation Package (VASP). The exchange–correlation interaction was described by generalized gradient approximation (GGA) with the Perdew–Burke–Ernzerhof (PBE) functional. The Brillouin zone was integrated with a Monkhorst–Pack 2×2×1 k-point grid and plane-wave energy cutoff of 520 eV for all calculations. Anatase (101)-(1×3), rutile (110)-(3×2) and Ce₂S₃ (001)-($\sqrt{2}\times\sqrt{2}$)R45° surfaces were built for adsorption energy calculations with DFT-D3 correction. A vacuum of 20 Å was used to eliminate interactions between periodic structures. Ce₂S₃ (001) surface was selected for simulation due to its lowest surface energy within the low-index facets (supplementary Table 1). The bottom half of atoms of the slab was fixed for structural relaxation. The convergence criteria for energy and force were 10⁻⁵ eV and 0.02 eV/Å, respectively. All the parameters were optimized in terms of accuracy and computational time using results of preliminary calculations. The adsorption energy (E_{ads}) of adsorbate on TiO₂ or Ce₂S₃ surface slabs is defined as $E_{\text{ads}} = E_{\text{slab+adsorbate}} - E_{\text{slab}} - E_{\text{adsorbate}}$, where $E_{\text{slab+adsorbate}}$, E_{slab} and $E_{\text{adsorbate}}$ are the energies of surface slab with adsorbate, surface slab and adsorbate, respectively. The work function is defined as $\Phi = E_{\text{V}} - E_{\text{F}}$, where E_{V} and E_{F} are the electrostatic potentials of the vacuum and Fermi levels, respectively.

Data Availability

The source data underlying Figures. 1d, 2a-c, 3c, 3e, 3f, 4, Supplementary Figures. 1, 2, 4–11, 13 and 17 are provided as a Source Data file, which is available in figshare with the identifier and in the Source Data file. All data are available from the corresponding author on request. Source data are provided with this paper.

Declarations

Acknowledgements

This work was supported by NSFC (51872220, 51961135303, 51932007, 21871217, 52073223, U1905215 and 52003213), the National Key Research and Development Program of China (2018YFB1502001) and the Fundamental Research Funds for the Central Universities (WUT: 2021IVB037). J.X. is grateful to the financial support by Australian Research Council. The project is also supported by the State Key Laboratory of Advanced Technology for Materials Synthesis and Processing (Wuhan University of Technology) (2018-KF-17).

Author contributions

F.X., J.X and J.Y. conceived and designed the experiments. F.X., K.M. and S.C. carried out the synthesis of the materials, the photocatalytic test and the characterizations of the materials. F.X. and C.J. performed the ultrafast TA measurements. F.X. carried out the DFT calculations. F.X., J.X. and J.Y. contributed to data analysis. J.X. and J.Y. supervised the project. F.X. wrote the manuscript. J.X and J.Y. revised and reviewed the manuscript. All authors discussed the results and commented on the manuscript.

Additional information

Supplementary Information accompanies this paper at xxx.

Competing interests: The authors declare no competing interests.

Reprints and permission information is available online at xxx.

Journal Peer Review Information: Nature Communications thanks the anonymous reviewers for their contribution to the peer review of this work. Peer reviewer reports are available.

Publisher's note: Springer Nature remains neutral with regard to jurisdictional claims in published maps and institutional affiliations.

References

1. Wei J., *et al.* Metal-Organic Capsules with NADH Mimics as Switchable Selectivity Regulators for Photocatalytic Transfer Hydrogenation. *J. Am. Chem. Soc.* **141**, 12707–12716 (2019).
2. Xi Z. W., *et al.* Visible-Light Photocatalytic Synthesis of Amines from Imines via Transfer Hydrogenation Using Quantum Dots as Catalysts. *J. Org. Chem.* **83**, 11886–11895 (2018).
3. Zhang L., *et al.* Highly active TiO₂/g-C₃N₄/G photocatalyst with extended spectral response towards selective reduction of nitrobenzene. *Appl. Catal. B-Environ.* **203**, 1–8 (2017).
4. Dai X., Xie M., Meng S., Fu X., Chen S. Coupled systems for selective oxidation of aromatic alcohols to aldehydes and reduction of nitrobenzene into aniline using CdS/g-C₃N₄ photocatalyst under visible light irradiation. *Appl. Catal. B-Environ.* **158–159**, 382–390 (2014).
5. Guo X., Hao C., Jin G., Zhu H. Y., Guo X. Y. Copper nanoparticles on graphene support: an efficient photocatalyst for coupling of nitroaromatics in visible light. *Angew. Chem. Int. Ed. Engl.* **53**, 1973–1977 (2014).
6. Naya S., Niwa T., Kume T., Tada H. Visible-light-induced electron transport from small to large nanoparticles in bimodal gold nanoparticle-loaded titanium(IV) oxide. *Angew. Chem. Int. Ed. Engl.* **53**, 7305–7309 (2014).
7. Tsutsumi K., Uchikawa F., Sakai K., Tabata K. Photoinduced Reduction of Nitroarenes Using a Transition-Metal-Loaded Silicon Semiconductor under Visible Light Irradiation. *ACS Catal.* **6**, 4394–4398 (2016).

8. Lavorato C., *et al.* Pd/TiO₂ doped faujasite photocatalysts for acetophenone transfer hydrogenation in a photocatalytic membrane reactor. *J. Catal.* **353**, 152–161 (2017).
9. Ma Y., Li Z. Coupling plasmonic noble metal with TiO₂ for efficient photocatalytic transfer hydrogenation: M/TiO₂ (M = Au and Pt) for chemoselective transformation of cinnamaldehyde to cinnamyl alcohol under visible and 365 nm UV light. *Appl. Surf. Sci.* **452**, 279–285 (2018).
10. Xu F., *et al.* Electrospun TiO₂-Based Photocatalysts. *Solar RRL* **5**, 2000571 (2021).
11. Marinho B. A., de Souza S. M. A. G. U., de Souza A. A. U., Hotza D. Electrospun TiO₂ nanofibers for water and wastewater treatment: a review. *J. Mater. Sci.* **56**, 5428–5448 (2021).
12. Xu F., Meng K., Cheng B., Yu J., Ho W. Enhanced Photocatalytic Activity and Selectivity for CO₂ Reduction over a TiO₂ Nanofibre Mat Using Ag and MgO as Bi-Cocatalyst. *ChemCatchem* **11**, 465–472 (2019).
13. Wang R., *et al.* Graphdiyne-modified TiO₂ nanofibers with osteoinductive and enhanced photocatalytic antibacterial activities to prevent implant infection. *Nat. Commun.* **11**, 4465 (2020).
14. Xu F., *et al.* Graphdiyne: A New Photocatalytic CO₂ Reduction Cocatalyst. *Adv. Funct. Mater.* **29**, 1904256 (2019).
15. Xu F., Zhu B., Cheng B., Yu J., Xu J. 1D/2D TiO₂/MoS₂ Hybrid Nanostructures for Enhanced Photocatalytic CO₂ Reduction. *Adv. Opt. Mater.* **6**, 1800911 (2018).
16. Kurnaravel V., Mathew S., Bartlett J., Pillai S. C. Photocatalytic hydrogen production using metal doped TiO₂: A review of recent advances. *Appl. Catal. B-Environ.* **244**, 1021–1064 (2019).
17. Mei Z., Wang G., Yan S., Wang J. Rapid Microwave-Assisted Synthesis of 2D/1D ZnIn₂S₄/TiO₂ S-scheme Heterojunction for Catalyzing Photocatalytic Hydrogen Evolution. *Acta Phys. -Chim. Sin.* **37**, 2009097 (2020).
18. Wang J., Wang G., Cheng B., Yu J., Fan J. Sulfur-doped g-C₃N₄/TiO₂ S-scheme heterojunction photocatalyst for Congo Red photodegradation. *Chin. J. Catal.* **42**, 56–68 (2021).
19. Xu Q., Zhang L., Cheng B., Fan J., Yu J. S-Scheme Heterojunction Photocatalyst. *Chem* **6**, 1543–1559 (2020).
20. Wageh S., Al-Ghamdi A. A., Jafer R., Li X., Zhang P. A new heterojunction in photocatalysis: S-scheme heterojunction. *Chin. J. Catal.* **42**, 667–669 (2021).
21. Wageh S., Al-Ghamdi A. A., Liu L. S-Scheme Heterojunction Photocatalyst for CO₂ Photoreduction. *Acta Phys. -Chim. Sin.* **37**, 2010024 (2020).
22. Zhu B., *et al.* Tuning the strength of built-in electric field in 2D/2D g-C₃N₄/SnS₂ and g-C₃N₄/ZrS₂ S-scheme heterojunctions by nonmetal doping. *J. Materiomics* **7**, 988–997 (2021).
23. Deng H., *et al.* S-scheme heterojunction based on p-type ZnMn₂O₄ and n-type ZnO with improved photocatalytic CO₂ reduction activity. *Chem. Eng. J.* **409**, 127377 (2021).
24. Shen R., *et al.* Tracking S-Scheme Charge Transfer Pathways in Mo₂C/CdS H₂-Evolution Photocatalysts. *Solar RRL* **5**, 2100177 (2021).

25. Chen C., *et al.* Perovskite LaNiO₃/TiO₂ step-scheme heterojunction with enhanced photocatalytic activity. *Appl. Surf. Sci.* **503**, 144287 (2020).
26. He F., Meng A., Cheng B., Ho W., Yu J. Enhanced photocatalytic H₂-production activity of WO₃/TiO₂ step-scheme heterojunction by graphene modification. *Chin. J. Catal.* **41**, 9–20 (2020).
27. Li X., *et al.* Enhanced photocatalytic degradation and H₂/H₂O₂ production performance of S-pCN/WO_{2.72} S-scheme heterojunction with appropriate surface oxygen vacancies. *Nano Energy* **81**, 105671 (2021).
28. Fei X., Tan H., Cheng B., Zhu B., Zhang L. 2D/2D Black Phosphorus/g-C₃N₄ S-Scheme Heterojunction Photocatalysts for CO₂ Reduction Investigated using DFT Calculations. *Acta Phys. -Chim. Sin.* **37**, 2010027 (2020).
29. Mao W.-X., *et al.* Core-shell structured Ce₂S₃@ZnO and its potential as a pigment. *J. Mater. Chem. A* **3**, 2176–2180 (2015).
30. Ranjith K. S., *et al.* Ce₂S₃ decorated ZnO-ZnS core-shell nanorod arrays: Efficient solar-driven photocatalytic properties. *Catal. Today* **278**, 271–279 (2016).
31. Chen S., Zhang H., Fu X., Hu Y. Preparation, characterization, and photocatalytic performance of Ce₂S₃ for nitrobenzene reduction. *Appl. Surf. Sci.* **275**, 335–341 (2013).
32. Zhang J., Tian J., Fan J., Yu J., Ho W. Graphdiyne: A Brilliant Hole Accumulator for Stable and Efficient Planar Perovskite Solar Cells. *Small* **16**, e1907290 (2020).
33. Xu F., Zhang J., Zhu B., Yu J., Xu J. CuInS₂ sensitized TiO₂ hybrid nanofibers for improved photocatalytic CO₂ reduction. *Appl. Catal. B-Environ.* **230**, 194–202 (2018).
34. Wang L., Cheng B., Zhang L., Yu J. In-situ Irradiated XPS Investigation on S-Scheme TiO₂@ZnIn₂S₄ Photocatalyst for Efficient Photocatalytic CO₂ Reduction. *Small* **17**, 2103447 (2021).
35. Cheng C., *et al.* An Inorganic/Organic S-Scheme Heterojunction H₂-Production Photocatalyst and its Charge Transfer Mechanism. *Adv. Mater.* **33**, 2100317 (2021).
36. Xu J. Y., *et al.* Ultrafast Dynamics of Charge Transfer and Photochemical Reactions in Solar Energy Conversion. *Adv. Sci.* **5**, 1800221 (2018).
37. Carlito S. Ponceca J., Pavel Cha bera, Jens Uhlig, Petter Persson, m V. S. Ultrafast Electron Dynamics in Solar Energy Conversion. *Chem. Rev.* **117**, 10940–11024.
38. Murthy D. H. K., *et al.* Origin of the overall water splitting activity of Ta₃N₅ revealed by ultrafast transient absorption spectroscopy. *Chem. Sci.* **10**, 5353–5362 (2019).
39. Rossi G., *et al.* Charge carrier dynamics and visible light photocatalysis in vanadium-doped TiO₂ nanoparticles. *Appl. Catal. B-Environ.* **237**, 603–612 (2018).
40. Yan Z., *et al.* Interpreting the enhanced photoactivities of 0D/1D heterojunctions of CdS quantum dots/TiO₂ nanotube arrays using femtosecond transient absorption spectroscopy. *Appl. Catal. B-Environ.* **275**, 119151 (2020).

41. Qian R., *et al.* Charge carrier trapping, recombination and transfer during TiO₂ photocatalysis: An overview. *Catal. Today* **335**, 78–90 (2019).
42. Liu H., *et al.* Graphene Grown on Anatase–TiO₂ Nanosheets: Enhanced Photocatalytic Activity on Basis of a Well-Controlled Interface. *J. Phys. Chem. C* **122**, 6388–6396 (2018).
43. Han C., *et al.* Beyond Hydrogen Evolution: Solar-Driven, Water-Donating Transfer Hydrogenation over Platinum/Carbon Nitride. *ACS Catal.* **10**, 9227–9235 (2020).
44. Xu J., Chen F., Xu X., Lu G.-P. The selective hydrogenation of nitroarenes and alkenes catalyzed by Pd@MOFs: The role of electronic interactions between Pd nanoparticles and MOFs on the reaction. *Mol. Catal.* **495**, 111157 (2020).
45. Nie R., *et al.* Platinum supported on reduced graphene oxide as a catalyst for hydrogenation of nitroarenes. *Carbon* **50**, 586–596 (2012).

Figures

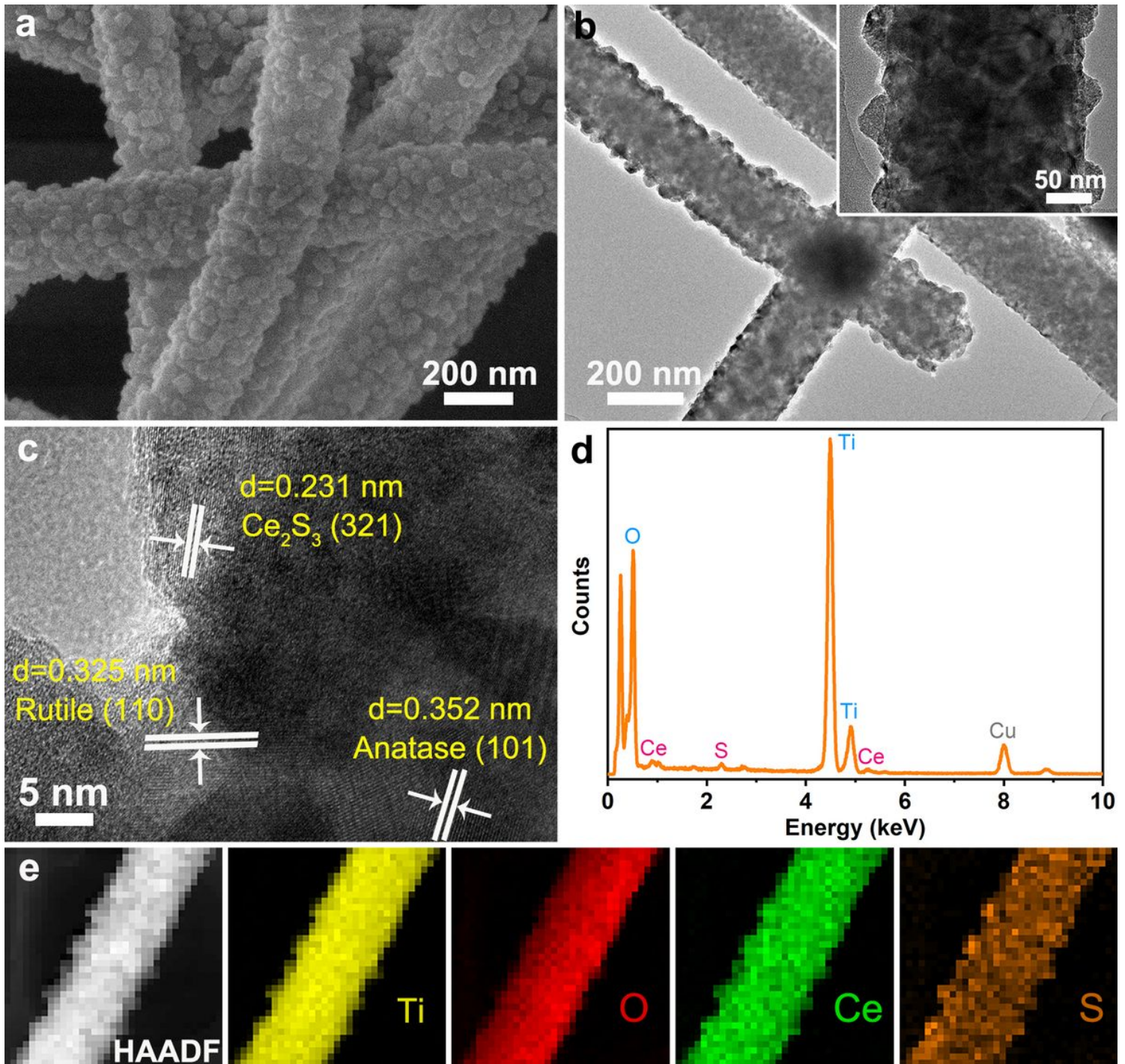


Figure 1

Morphology and structure of TiO₂/Ce₂S₃ heterojunction. a FESEM, b TEM and c HRTEM images of TC5. d EDX spectrum of TC5. e HAADF image and EDX elemental mappings of Ti, O, Ce and S elements in TC5.

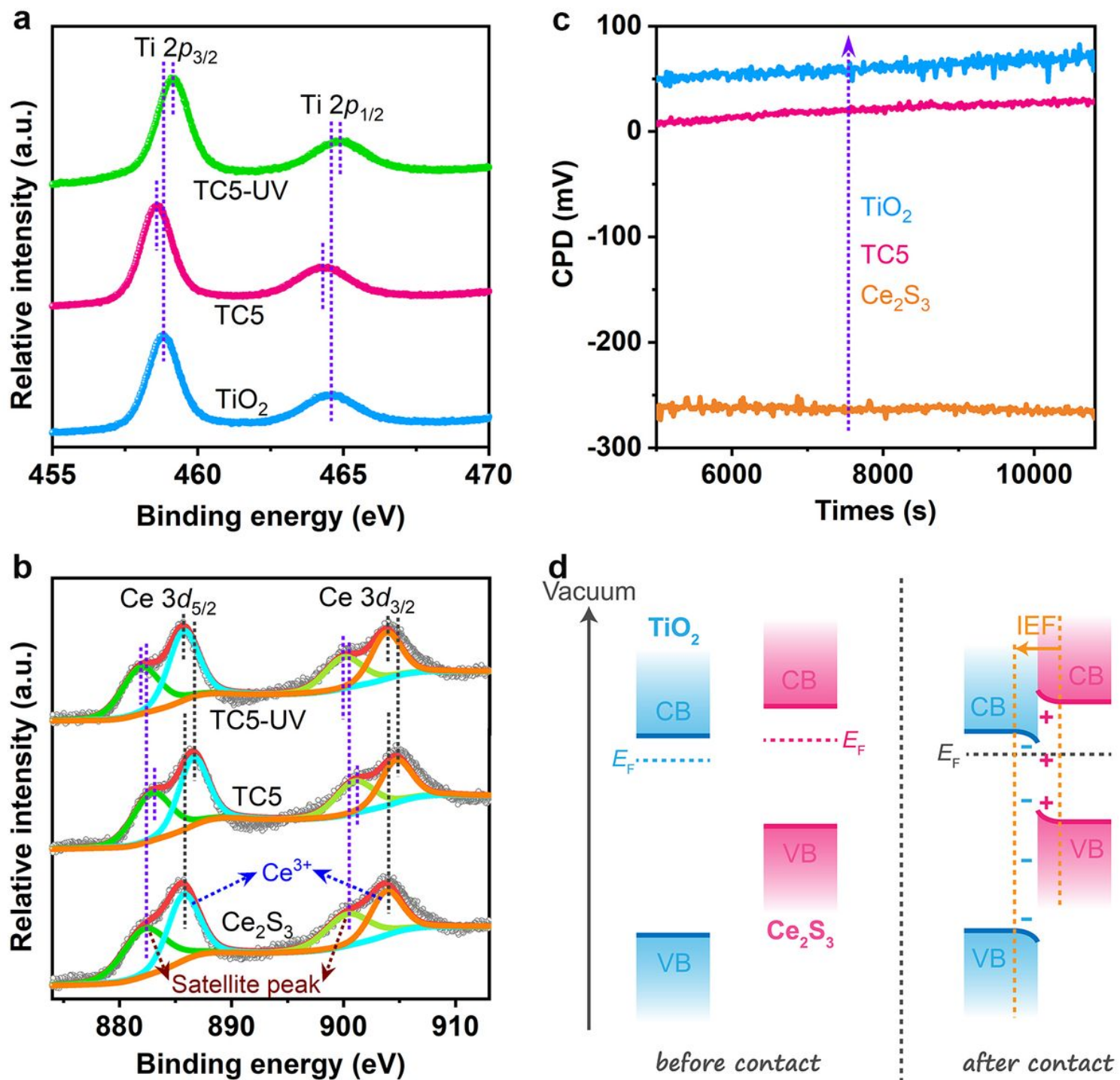


Figure 2

Electron transfer between TiO₂ nanofibers and Ce₂S₃ nanoparticles. High resolution XPS spectra of a Ti 2p and b Ce 3d of TiO₂, Ce₂S₃ and TC5. In-situ XPS spectra were collected under UV-vis light irradiation. c CPD profile of TiO₂, TC5 and Ce₂S₃ under dark condition. d The band structure of TiO₂ and Ce₂S₃, as well as the schematic diagram for the electron transfer and the formation of IEF between TiO₂ and Ce₂S₃ upon contact.

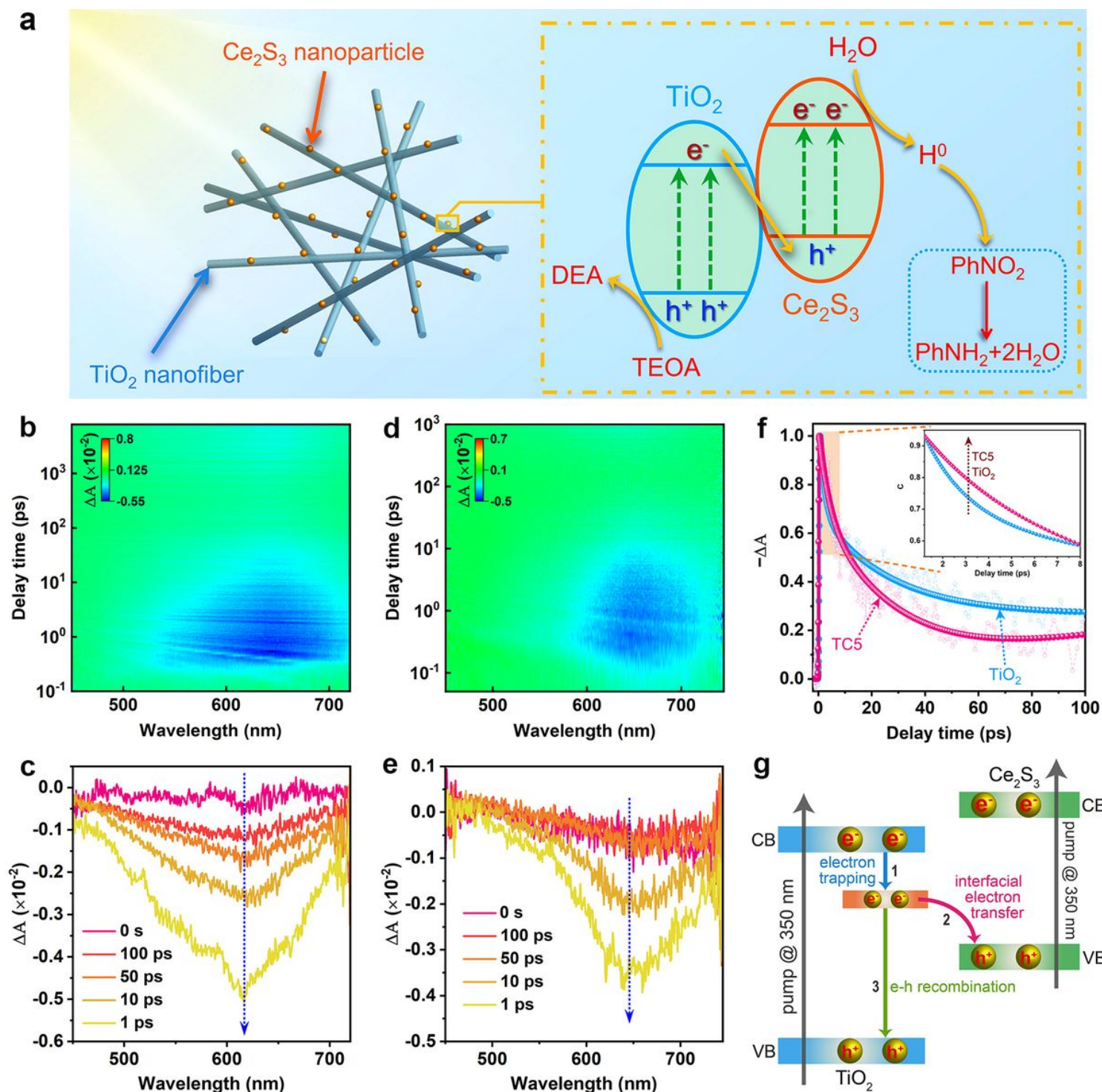


Figure 3

Insights into the charge separation mechanism of S-scheme heterojunction. a Schematic illustration of TiO₂/Ce₂S₃ S-scheme heterojunction under UV light irradiation for photocatalytic nitrobenzene hydrogenation. The pseudocolor plots and transient absorption spectra recorded at indicated delay times measured with 350 nm excitation: b, c pure TiO₂ nanofibers and d, e TiO₂/Ce₂S₃ nanohybrids (TC5). f The corresponding transient absorption kinetic traces of TiO₂ and TC5 at 645 nm within 100 ps. g Schematic illustration of the charge transfer mechanism in the TiO₂/Ce₂S₃ composite system.

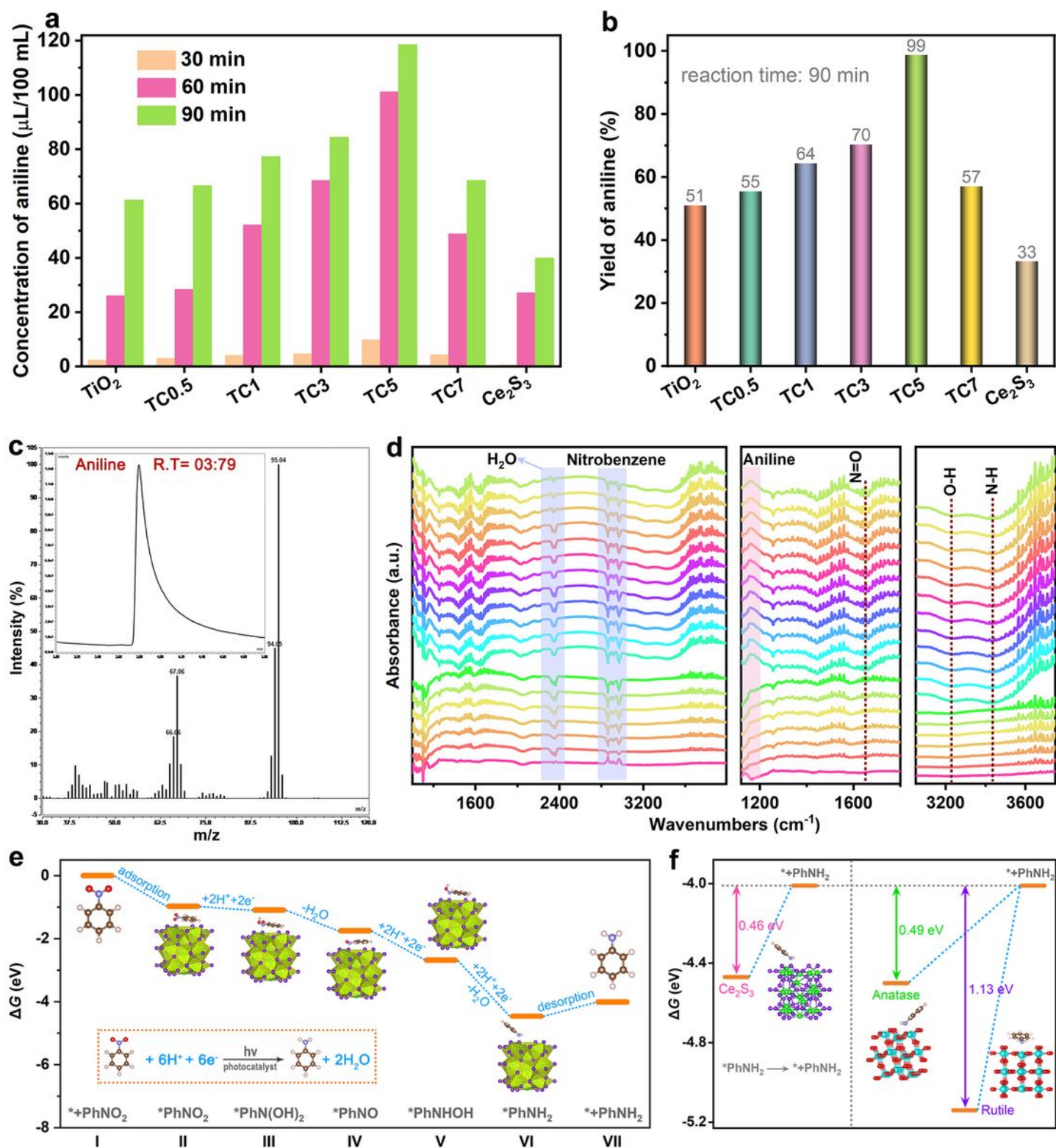


Figure 4

Performance and mechanism insights into photocatalytic hydrogenation reaction. Photocatalytic activities of nitrobenzene hydrogenation over TiO_2 , TC_x and Ce_2S_3 under UV light irradiation: a time course of the concentration of aniline, b the yield of aniline at the light irradiation time of 90 min catalyzed by different photocatalysts. c Mass spectra of the aniline product and total ion chromatography (inset) obtained by using D_2O (not H_2O) as hydrogen source for the photocatalytic

nitrobenzene hydrogenation over TC5. d In-situ DRIFTS spectra on the TC5 for the adsorption of a mixture of H₂O and nitrobenzene vapor for 60 min in dark and photo-irradiation for another 120 min; the signals were recorded every 10 minutes. e Gibbs free energy diagram of the photocatalytic hydrogenation of nitrobenzene to produce aniline over Ce₂S₃ (001) slab. f Gibbs free energy change of the aniline product desorbing from anatase TiO₂ (101), rutile TiO₂ (110) and Ce₂S₃ (001) slabs, with the free energy of each slab combined with free PhNO₂ as the reference. The cyan, red, green, violet, light pink, brown and blue spheres stand for Ti, O, Ce, S, H, C and N atoms, respectively.

Supplementary Files

This is a list of supplementary files associated with this preprint. Click to download.

- [SupplementaryInformation.docx](#)